

The Determination of the Rotational State and Interior Structure of Venus with VERITAS

Gael Cascioli¹, Scott Hensley², Fabrizio DE MARCHI¹, Doris Breuer³, Daniele Durante⁴, Paolo Racioppa⁴, Luciano Iess⁵, Erwan Mazarico⁶, and Suzanne E. Smrekar²

¹Sapienza University of Rome

²Jet Propulsion Laboratory

³German Aerospace Center

⁴Sapienza Università di Roma

⁵Università di Roma La Sapienza

⁶NASA Goddard Space Flight Center

November 22, 2022

Abstract

Understanding the processes that led Venus to its current state and will drive its future evolution is one of the main challenges of the next generation of space missions. In this work we analyze the retrieval of the spin vector, the tidal response and the moment of inertia of Venus with VERITAS, a Discovery-class mission proposed to NASA. By simulating the joint analysis of Doppler tracking data and tie points provided by the onboard synthetic aperture radar, we show that VERITAS would provide strong constraints on the interior structure of the planet. In particular we show that VERITAS would provide accuracies in the estimates of the tidal Love number k_2 to 3.9×10^{-4} , its tidal phase lag to 0.04° , and the moment of inertia factor to 1.4×10^{-3} (0.4% of the expected value).

21 **Abstract**

22 Understanding the processes that led Venus to its current state and will drive its future evolution
23 is one of the main challenges of the next generation of space missions. In this work we analyze
24 the retrieval of the spin vector, the tidal response and the moment of inertia of Venus with
25 VERITAS, a Discovery-class mission proposed to NASA. By simulating the joint analysis of
26 Doppler tracking data and tie points provided by the onboard synthetic aperture radar, we show
27 that VERITAS would provide strong constraints on the interior structure of the planet. In
28 particular we show that VERITAS would provide accuracies in the estimates of the tidal Love
29 number k_2 to 3.9×10^{-4} , its tidal phase lag to 0.04° , and the moment of inertia factor to
30 1.4×10^{-3} (0.4% of the expected value).

31

32 **Plain Language Summary**

33 Understanding the processes that led Venus to its current state and will drive its future evolution
34 is one of the main challenges of the next generation of space missions. VERITAS is a Discovery-
35 class mission to Venus proposed to NASA which may be selected in the spring of 2021. In this
36 work we simulate and analyze the capability of VERITAS of measuring geophysical parameters
37 that are crucial to shed light on many open questions about our neighboring planet. We show that
38 the measurements VERITAS will gather, would provide strong and new evidences about the
39 interior structure of the planet and determine the state of the core (solid/liquid) its composition
40 and the viscosity and composition of the mantle.

41 **1 Introduction**

42 The most comprehensive mapping of Venus was done by the Magellan mission in the early
43 1990s (Saunders et al., 1992). To succeed in its scope, Magellan employed a combination of
44 Doppler tracking data and S-band Synthetic Aperture Radar (SAR), altimeter and radiometer to
45 make nearly global observations of the surface of Venus (Ford & Pettengill, 1992). Magellan in-
46 situ observations led to the most accurate estimate of the planet's spin axis orientation and sidereal
47 rotation period (Davies et al., 1992, see also Campbell et al., 2019 for a resume of several
48 observation campaigns), gravity field and tidal response (Konopliv et al., 1999; Konopliv & Yoder,
49 1996). The Magellan estimates, however, proved not sufficiently precise to constrain the interior
50 structure. As shown in Dumoulin et al., (2017), current estimates of the tidal response do not
51 distinguish between a liquid and solid core and the absence of a measurement of the tidal phase
52 lag prevents from inferring the viscous response of the interior. Moreover, without direct
53 observations of the moment of inertia factor ($MOIF = C/MR^2$ where C is the polar moment of
54 inertia and M, R the planetary mass and radius, respectively), no constraints can be placed on the
55 internal density profile and core size. Thus, models of Venus' interior rely on scaling Earth's
56 interior structure to Venus' radius (e.g., Yoder, 1995; Aitta, 2012).

57

58 The Venus Emissivity, Radio science, INSAR, Topography And Spectroscopy (VERITAS)
59 mission (Smrekar et al., 2021; Freeman et al., 2015) is a partnership led by NASA/JPL between
60 US scientists and engineers, with strong collaborations and contributions of the German, Italian
61 and French Space Agencies. It is one of four candidate NASA Discovery 2019 missions selected
62 for a Concept Study Phase, expected to lead to a selection by NASA in the spring of 2021.

63

64 Among the main scientific objectives of VERITAS, the determination of the tidal response, tidal
65 phase lag and MOIF are specifically focused at pushing forward our understanding of the Venus
66 interior. VERITAS would carry two science instruments: VISAR (Venus Interferometric Synthetic
67 Aperture Radar), the X-band interferometric radar (Hensley et al., 2020); and VEM, an infrared
68 spectroscopic mapper (Helbert et al., 2020). Data from VISAR would be combined with two-way
69 dual X- and Ka-band Doppler tracking data provided by the onboard telecom subsystem and used
70 to improve estimates of the Love number k_2 , the tidal phase lag δ_{k_2} and the MOIF in order to
71 constrain the structure of the Venus interior.

72
73 Arriving at Venus after a 9-month cruise, VERITAS would begin an 11-month aerobraking phase,
74 paused after 5 months for 5 months of VEM science observations, before continuing to its final
75 nearly circular polar orbit (180 x 255 km in altitude). VERITAS plans to operate for 4 Venus
76 sidereal days (or 4 cycles, 243 Earth days each), providing a nearly global coverage of the planet
77 for all its investigations (gravity science, VISAR, and VEM).

78
79 The goal of this work is to simulate the operational scenario of VERITAS' gravity experiment to
80 assess the accuracy in the estimate of k_2 , δ_{k_2} and MOIF. This paper is structured as follows: in
81 section 2 we describe the concept and the assumptions used in our simulations for both Doppler
82 and radar measurements (sec 2.1 and 2.2 respectively); in section 3.1 we detail the methodology
83 for the estimation of the MOIF, and discuss the simulation setup and observational scenario in
84 section 3.2; in section 4 we present and discuss the results of the simulations; section 5 follows
85 with concluding remarks.

86 **2 Methods**

87 It is well known that the sole knowledge of the gravitational field is not enough to infer the
88 moments of inertia of a planet, which provide crucial constraints on its interior structure. To
89 constrain the inertia tensor of a body, the gravity field information must be complemented by
90 measurements of the rotational state. Precise Doppler tracking data, the primary observable
91 quantity for gravity field recovery, are quite sensitive to the rotational state of the planet, but the
92 attainable accuracy can be improved by augmenting the analysis with surface feature tracking. The
93 latter provides direct observations of the rotational motion of the planet by measuring the inertial
94 displacement of physical features located on the planet's surface. In this work, we make use of a
95 combined processing of Earth-spacecraft Doppler tracking data and repeated surface landmark
96 observations (tie points) provided by the onboard interferometric SAR.

97 **2.1 Spacecraft Doppler Tracking**

98 Doppler measurements are the primary observables for reconstructing the orbit of the
99 spacecraft and recovering the gravity field of a planet. These measurements are collected by
100 recording the Doppler shift of a radio signal sent from the ground station to the spacecraft, which
101 then coherently retransmits it back to the Earth by means of an onboard transponder (two-way
102 configuration). VERITAS' Doppler tracking system, with its heritage from ESA's BepiColombo
103 (Iess et al., 2009, Iess et al., 2021), is able to establish two simultaneous coherent radio links in the
104 X and Ka bands and to provide measurements of the range-rate of the probe with an accuracy of
105 0.018 mm/s (Ka band, 10s integration time) under nominal operational conditions (Cappuccio et
106 al., 2020). The dual band configuration can be used near superior solar conjunctions to suppress

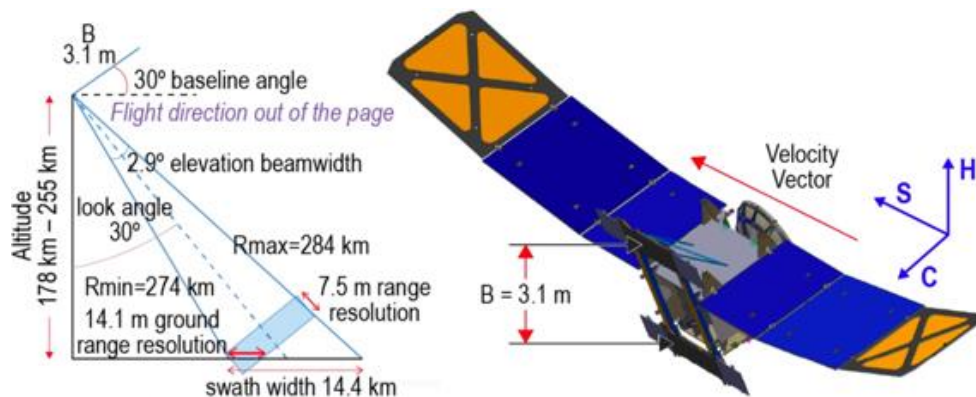
107 about 75% of the noise due to charged particles in the solar corona (Bertotti et al., 1993). In
 108 addition, the tracking system is capable of range measurements at the level of 2-3 cm at Ka band.
 109

110 The operational scenario of VERITAS consists of five to seven Doppler tracking passes a week,
 111 collected by NASA's Deep Space Network ground stations. The VERITAS observation schedule
 112 entails approximately a daily contact to ground for 8 hours, and 16 hours of VISAR observations.
 113 For the gravity experiment we simulate 8-hour passes for five days a week collected by DSS 25
 114 (Goldstone, CA), a station of the NASA Deep Space Network, with a white gaussian noise with
 115 standard deviation of 0.018 mm/s, removing data having an elevation angle below 15° and
 116 accounting for occultation periods. The integration time of synthetic Doppler observables is set to
 117 10 s, which is sufficient to resolve gravity field features as small as 190 km after 4 cycles.

118 2.2 Radar Observations and Tie Points

119 The VERITAS orbit is designed to have overlapping ground tracks from cycle to cycle to
 120 enable repeating passes for radar interferometric observations. Radar data are collected on 11 out
 121 of 16 orbits per day, and downlinked to Earth on the remaining 5 orbits, when two-way X and Ka
 122 band tracking data are acquired. Therefore, radar and Doppler data are not collected
 123 simultaneously.

124 VISAR is an X-band interferometric radar operating at 7.9 GHz (3.8 cm wavelength) and has a
 125 20 MHz bandwidth from which radar imagery with 30 m ground resolution pixels and
 126 topographic data with 250 m spatial resolution and ~ 5 m elevation accuracy is produced. The
 127 radar acquires data with a look angle of 30° (angle between the antenna boresight and spacecraft
 128 nadir) and images a swath width of 14.4 km (Figure 1). After an orbital period, planetary rotation
 129 shifts the VERITAS ground tracks by roughly 10 km; thus, the swath width provides more than 2
 130 km of overlap between swaths acquired on adjacent orbits, enabling coherent mapping of Venus
 131 surface.



132

133 **Figure 1.** VISAR flight configuration and observing geometry.

134 VISAR transmits pulses and records the received echoes to generate images of the backscattered
 135 signal from the surface. To achieve fine resolution in the radar along-track or azimuth direction,
 136 SAR image formation combines echoes from multiple pulses when a point is illuminated by the
 137 radar antenna beam. The pixel location in a radar image is determined by the range, i.e., distance

138 from the platform to the pixel, and the Doppler frequency, i.e., projection of spacecraft velocity
139 on the line-of-sight. For Venus, the range, derived from the delay between pulse transmit time
140 and echo return time, must be corrected for the delay induced by the thick Venus atmosphere.
141 Atmospheric contribution amounts to 200-400 m of additional range, depending on the pixel
142 elevation and imaging geometry. Since VISAR is an interferometer, it solves for the 3-
143 dimensional position of each pixel using the range, Doppler and interferometric phase from two
144 spatially separated antennas. Surface features (landmarks) imaged on multiple orbits can be
145 identified using automated matching software.

146 To include radar tie points in our simulations, we generated a simulated dataset of radar
147 observations. Two classes of radar tie points were simulated. The first class of radar tie points
148 (*local tie points*) are observed in the swath overlap region of adjacent orbits. These
149 measurements would allow to better determine the trajectory of the probe by providing
150 constraints between adjacent orbits when VERITAS is not tracked by the DSN. The second class
151 of radar tie points are the so-called *global tie points*. A point on the surface can in principle be
152 imaged up to 8 times (excluding swath overlaps) during the 4-cycle mission: one time each on
153 the descending and ascending passes, for each of the four cycles. Each observation is separated
154 by half a Venus sidereal period thus enabling to place tight constraints on the inertial motion of
155 surface features, directly related to the rotational state of the planet.

156 For the simulation, we placed global tie points on a latitude/longitude grid with approximately
157 150 km spacing separating points in both directions. We exclude orbits that are used for data
158 downlink, in solar conjunction or in power-restricted orbits where data is not collected. The
159 relative range and Doppler measurement errors depend on how accurately imagery acquired from
160 different orbits can be matched. SAR image matching is hindered by speckle that results in a
161 grainy appearance due to the coherent nature of imaging and from differences in imaging
162 geometry, either incidence angle or look direction. Matching accuracy is a function of the image
163 signal-to-noise ratio, the number of looks used to reduce both speckle and thermal noise, imaging
164 geometry differences and the amount of scene contrast (see section S4).

165 Identification of radar tie points would use an automated scene matching algorithm. The
166 automated matching algorithm computes the cross correlation for a search window that covers
167 the largest expected offset due to ephemeris errors.

168 To account for the spatially variable nature of the matching accuracy, and the consequent range
169 and Doppler measurement error, we adopt the match covariance matrix used in the automated
170 matching algorithm to estimate the matching accuracy (Frankot et al., 1994). We tune the
171 matching metric based on match accuracy statistics from Magellan stereo data that covered
172 approximately 20% of the surface (for additional details see section S4).

173 The average accuracy of the range and Doppler observations of each radar tie point is 3 m and 10
174 Hz derived from an average 0.2 pixel matching accuracy using a 64×64 matching window of 30

175 m resolution pixel imagery where each pixel corresponds to 15 m of range and 40 Hz of Doppler.
 176 A total of 710,496 tie points were simulated corresponding to 43,980 unique landmarks.

177

178 **3 Numerical Simuations**

179 3.1 Determination of the Moment of Inertia from the Rotational State

180 The torque of the Sun on Venus determines the precession of its spin axis in a conical
 181 motion about the orbit normal. The precession rate Ω is:

$$182 \quad \Omega = \frac{3}{2} \frac{n^2}{\omega} \cos \epsilon \frac{J_2}{k} \quad (1)$$

183 where J_2 is the un-normalized degree 2 zonal coefficient of the gravity field of Venus, k is the
 184 MOIF, ω is the sidereal spin rate, n is the mean motion and ϵ the obliquity (angle between spin
 185 axis and orbit normal). If a measurement of the precession rate of the spin axis is available,
 186 Equation (1) can be used to estimate the MOIF of the planet. The precession of Venus, deduced
 187 from Equation (1), has a period of ~ 29.000 yr (Cottureau & Souchay, 2009) for reasonable
 188 ranges of MOIF values. Although Ω is relatively large (during the 4 Venus cycles spanned by
 189 VERITAS the angular displacement of the pole is about 0.03°) relative to the small axial tilt of
 190 the planet (2.64°), the physical displacement of the pole on Venus surface corresponds to only
 191 151 m. Note that the attainable accuracy on the MOIF primarily results from the accuracy of the
 192 precession rate, since J_2 and the other quantities in Eq. (1) are much better known.

193 As the precession period is much longer than the VERITAS observations, the precessional
 194 motion of Venus can be described by three first-degree polynomials for the spin vector right
 195 ascension, $\alpha(t) = \alpha_0 + \dot{\alpha}(t - t_0)$, declination $\delta(t) = \delta_0 + \dot{\delta}(t - t_0)$, and prime meridian,
 196 $w(t) = w_0 + \frac{2\pi(t-t_0)}{T_{sid}}$, with t_0 corresponding to the J2000 epoch and T_{sid} being the sidereal
 197 period (see e.g., Archinal et al. 2009). The precession constant Ω can be directly associated
 198 (under the assumption of negligible nutations and small deviation from the reference position, as
 199 shown in the supporting information S3) to $\dot{\alpha}$ and $\dot{\delta}$ as:

$$200 \quad \Omega = c_1 \dot{\alpha} = c_2 \dot{\delta} \quad (2)$$

201 with the coefficients c_1 and c_2 determined by the orbital inclination of Venus, the reference
 202 position of the pole (α_0, δ_0) and the longitude of the orbital node at the reference epoch. In our
 203 simulations we therefore estimate the pole polynomial coefficients and exploit the
 204 aforementioned procedure to assess the uncertainty on Ω and thus on the MOIF.

205 To verify the validity of our approach, we have developed a more detailed (and computationally
 206 expensive) model of Venus's rotational state, based on the numerical integration of the Euler
 207 equations for the rigid body, taking into account the gravitational torques exerted on Venus by all
 208 the main solar system bodies. This model directly embeds the dependence from the inertia tensor
 209 and its relationship with gravity field quadrupole coefficients (via the McCullagh formula;
 210 Murray & Dermott, 2000), yielding a direct estimate of the MOIF. We verified that the results

211 obtained under the linear assumption are in very good agreement with the numerically integrated
212 model and thus opted for the former for the sake of reducing the computational effort.

213 3.2 Simulation Setup and Scenario

214 To assess the capabilities of VERITAS to retrieve the rotational state, Love numbers and MOIF
215 we conducted an extensive set of numerical simulations replicating the nominal operational
216 scenario of VERITAS.

217 We randomly downsampled the full set of simulated landmarks to ~8000. The choice of
218 simulating only a subset of landmarks is supported by two arguments. Firstly, observations of a
219 landmark-dense area might be highly correlated. Selecting only well-spaced points justifies the
220 assumption that the observations are statistically independent, therefore simplifying the analysis.
221 Secondly, the outcome of the simulation can be considered as a conservative estimate of what
222 would be possible if the entire dataset is processed (for a discussion on the influence of the
223 number of measured landmarks refer to the supporting information S1).

224 We assessed the capabilities of VERITAS through a covariance analysis. Using the JPL orbit
225 determination software MONTE (Evans et al., 2018), we integrate the trajectory of the probe,
226 generate synthetic Doppler and VISAR data according to the assumptions outlined in Sec. 2.1
227 and 2.2, add white gaussian noise (according to the expected noise levels, 0.018 mm/s for Earth-
228 spacecraft Doppler tracking and 3m and 10Hz for the radar tie points in range and Doppler
229 respectively) and combine all the data in a least squares filter (ORACLE) developed at Sapienza
230 University and validated with several space missions (e.g., Iess et al., 2018). The practical
231 implementation of the combined processing procedure is straightforward. The tie points
232 measurements, being in the form of range and range-rate do not require special handling and can
233 be directly used in the orbit determination least squares batch filter. We used this estimation
234 technique, together with the multiarc approach that is best suited for data analysis of long
235 duration gravity experiments (e.g., Durante et al., 2020; Mazarico et al., 2014; Konopliv et al.,
236 2013).

237 The dynamical model used to propagate the spacecraft trajectory includes the monopole
238 gravitational acceleration of all main solar system bodies, a degree and order 50 static gravity
239 field of Venus (derived from Konopliv et al., 1999 - we limit the spherical expansion to degree
240 50 since higher degrees have negligible effects on the results for the parameters of interest), the
241 tidal response to the Sun and the atmospheric thermal tides, the non-gravitational accelerations
242 due to solar radiation pressure and atmospheric drag. Density variations, depending on local time
243 and solar activity (Müller-Wodarg et al., 2016, Kliore et al., 1992), induce accelerations on the
244 spacecraft over typical time scales ranging from half to a quarter of the orbital period. It is a
245 common procedure for the orbit determination of orbiters around thick-atmosphere planets to
246 account for the unpredictable short-term variability of the drag acceleration by modeling the drag
247 coefficient C_d as a time-varying parameter with time update depending on the time scale of the
248 atmospheric phenomena. In our simulations we chose to model a time-varying C_d by estimating a
249 set of piece-wise constant along-track accelerations with a time update of 30 minutes.

250 Our model includes also atmospheric thermal tides as the spacecraft tracking system will be
251 sensitive to their effect (Goossens et al., 2018, Bills et al., 2020). The numerical results we report

252 in the next paragraphs are based on the assumption of a knowledge of the atmospheric pressure
 253 model with an initial 10% accuracy. Thermal tides modeling and the effect of the assumed a
 254 priori knowledge on the final results is discussed in S2.

255 We run the described filter solving for the set of parameters of interest. In our multiarc approach,
 256 the tracking data are subdivided in 2.5-day arcs and the parameters are divided in two sets: local
 257 parameters (those affecting a single arc, e.g. position and velocity of the probe) and global
 258 parameters (parameters affecting all the arcs, e.g. the gravity field of the planet). The complete
 259 list of parameters comprises the state of the probe, empirical along-track accelerations, Venus
 260 gravity field spherical harmonics coefficients up to degree and order 50, complex Love number
 261 of degree 2, the Venus pole location (right ascension, declination) and its precession rate, the
 262 Venus sidereal period, the thermal tide-induced gravity field correction coefficients (as detailed
 263 in S2) and the coordinates of each of the observed landmarks (latitude, longitude, altitude), for a
 264 total of 27,320 global parameters.

265

266 **4 Results and Discussion**

267 Table 1 reports the uncertainties (all results in tables and text, unless otherwise stated, are
 268 three times the formal uncertainty) attainable for the Venus rotational parameters, the Love
 269 number and the MOIF in the nominal VERITAS mission configuration in two cases: Doppler
 270 tracking data only, and Doppler tracking data combined with VISAR observations. The inclusion
 271 of VISAR tie point measurements in the orbit determination enables a large improvement in the
 272 determination of the rotational state of Venus, not attainable with Doppler data alone. The tie
 273 points increase the accuracy in the pole location and MOIF by about a factor of 6, while a
 274 smaller improvement (~ 2.5) is found on k_2 and its tidal phase lag.

275 The current estimate of Venus Love number (0.295 ± 0.066 , 2σ , Konopliv & Yoder 1996),
 276 coupled with the lack of a magnetic field, does not allow resolving between a liquid and solid
 277 core (Dumoulin et al., 2017, see figure 2). Dumoulin et al. (2017) determined that the state of the
 278 core and its size, as well as the viscous response of the interior, can be well constrained with a
 279 knowledge of k_2 to an accuracy smaller than 3% (0.01) and phase lag $\sigma_{\delta_{k_2}} < 0.25^\circ$.

280 Our simulations show that VERITAS will be able to determine these tidal quantities with an
 281 accuracy substantially better than these threshold values. Right ascension and declination of the
 282 pole (α_0 and δ_0) can be determined with an accuracy increased by an average factor of 6,
 283 improving the results obtained by Magellan by more than 100 times. A comparable improvement
 284 is found for the obliquity ϵ ($\sigma_\epsilon = 160 \text{ mas}$). VERITAS will also enable the determination of the
 285 precession rate Ω to a level of 5.1×10^{-3} deg/century, which allows the retrieval of the MOIF
 286 (with the procedure and constraint detailed in Sec 3.1 and S3). This would be the first dynamical
 287 measurement of Venus MOIF resulting in an accuracy of 0.4% of its predicted central value
 288 (0.336, Cottureau & Souchay, 2009). The accurate measurement of the MOIF provides an

289 additional, strong constraint to improved models of the Venus interior, by reducing the
290 uncertainty in the density of the core and the mantle.

291 Based on current models (Dumoulin et al., 2017) the constraints on k_2 and δ_{k_2} can determine
292 core state, and core size to within 100 km and average mantle viscosity to within an order of
293 magnitude (See Figure 2). The latter value strongly depends on the temperature distribution and
294 the volatile content in the mantle and therefore provides information about the heat and volatile
295 loss of the planet. For example, a warm and wet mantle, representative of a planetary interior
296 that has not cooled much and has lost little of its original water, has a low viscosity, while a cold
297 and dry mantle, representative of an efficiently cooled and outgassed interior, has a high
298 viscosity. These two extreme models would differ in viscosity by several orders of magnitude
299 and could be distinguished in measuring the phase lag.

300 Different formation scenarios lead to different compositional models based on cosmochemical
301 assumptions and trends among Earth-like planets to model the interior of Venus. A major
302 difference in the models is the FeO content of the mantle, which can vary between 0.42 and 18.7
303 wt. %. This results in different values of MOIF ranging between 0.33 and 0.342 (~3 %
304 variation), with otherwise the same assumption about the thermal state and the core composition
305 (Dumoulin et al., 2017). Knowledge of the MOIF with an accuracy of 0.4% will therefore
306 further help to distinguish the mantle composition models.

307 The amount of light elements in the core, particularly important for a better understanding of
308 Venus' magnetic field evolution and also informative about Venus' conditions during core
309 formation, is not known. The two parameters together, k_2 and MOIF, help to better distinguish
310 the models as has already been shown, for example, for Mars (Rivoldini et al. 2011). The
311 information about the density distribution from the MOIF is not unique, i.e. for the same MOIF
312 the core can be small and dense or relatively larger and lighter. If the core of Venus is liquid, the
313 core size can be constrained independently with k_2 and thus in combination of MOIF also the
314 core density.

315 All these fundamental quantities, such as core state, size and composition, mantle composition
316 and viscosity, are necessary to understand the formation of Venus and its thermal and magnetic
317 evolution. They serve, for example, as inputs (core radius and core and mantle composition) or
318 constraints (core state and present effective mantle viscosity) for modelling core and mantle
319 processes and the thermal and magnetic evolution.

320 VERITAS would also provide a tight constraint on the sidereal rotation period of Venus (T_{sid}) at
321 the sub-second level ($\sigma_{T_{sid}} = 0.13$ s).

322 As a by-product of the estimation process, we can determine the location of all observed
323 landmarks, thus providing the backbone of an accurate geodetic control network. The median
324 values of the recovered landmark position accuracy in altitude, latitude and longitude (mapped
325 on the reference surface of Venus) are respectively $M_{alt} = 3$ m, $M_{lat} = 9$ m, $M_{lon} = 12.6$ m.
326 The determination of the landmark positions allows also to retrieve the radial displacement
327 associated to the tidal forcing, parametrized by the Love number h_2 . The retrieved uncertainty

328 ($\sigma_{h_2} = 0.195$, corresponding to ~ 12 cm of maximum radial displacement) allows to determine h_2
 329 to 25-45% of its predicted value (0.45-0.75 Dumoulin et al., 2017).

330 The inclusion of tie points improves the orbital solution by providing observability during
 331 periods in which the spacecraft is not tracked from the Earth. This aspect is particularly
 332 important for providing a uniform tracking coverage along the orbit and giving robustness to the
 333 determination of physical effects such as atmospheric drag whose variability cannot be predicted
 334 with enough accuracy by a deterministic a priori model. The denser availability of orbit-related
 335 data is also the reason for a slight enhancement of the low-degree gravity field retrieval, since it
 336 allows a better resolution of the large spatial scales (i.e., low degree) of the planetary
 337 gravitational field. The improvement of the static gravity field determination is strictly related to
 338 the improvement of the (complex) Love number.

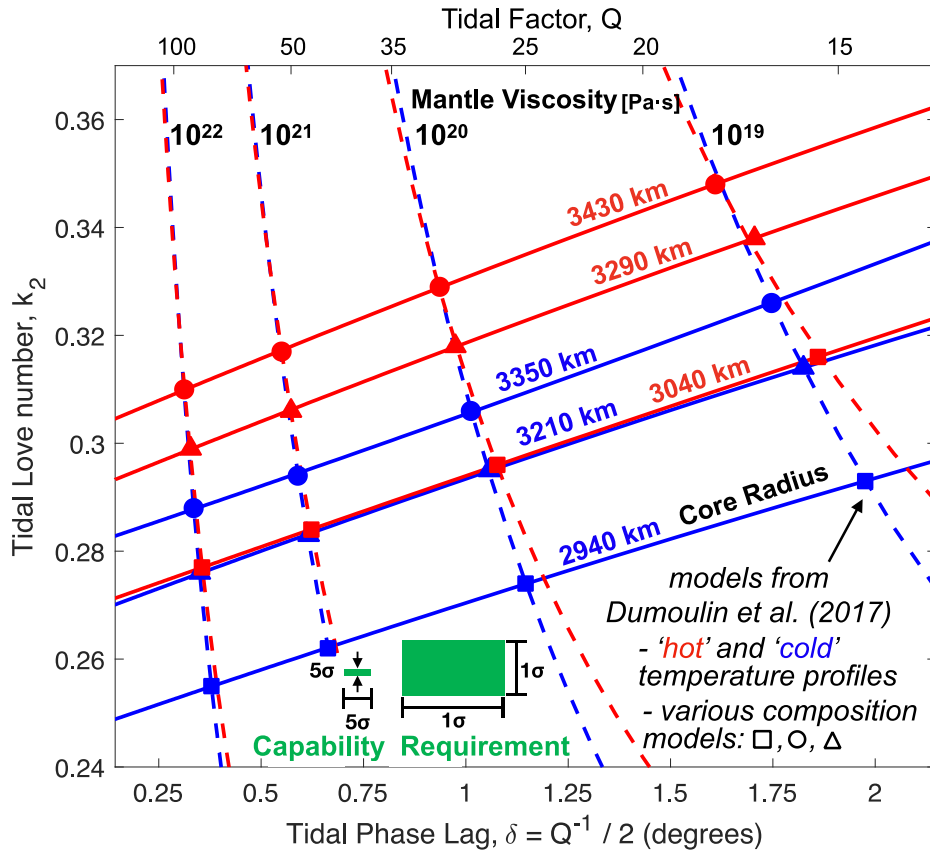
339 **Table 1** Results of the numerical simulations. We report the uncertainties in the two cases of Doppler
 340 only and Doppler + Tie points analyses (three times the formal uncertainty). The tie points improvement
 341 factor is the ratio between the uncertainties obtained without and with the inclusion of VISAR data.

342

Parameter	Current uncertainty from observations	Source	Earth Doppler Only	Earth Doppler + Tie Points	Tie Points Improvement Factor
α_0 [arcsec]	72	Davies et al., 1992	2.3	0.36	6.3
δ_0 [arcsec]	36		1.3	0.21	6.2
T_{sid} [day]	1×10^{-4}		1.1×10^{-5}	1.5×10^{-6}	7.1
ϵ [arcsec]	30	Derived from Davies et al., 1992	1.0	0.16	6.3
Ω [deg/century]	-	-	3.2×10^{-2}	5.1×10^{-3}	6.3
$MOIF$	-	-	8.6×10^{-3}	1.4×10^{-3}	6.3
k_2	6.6×10^{-2}	Konopliv and Yoder, 1996	9.6×10^{-4}	3.9×10^{-4}	2.5
δ_{k_2} [deg]	-	-	8.6×10^{-2}	4.0×10^{-2}	2.1

343

344



345
 346 **Figure 2** The required uncertainty on Love number k_2 and the tidal phase lag to constrain core radius
 347 and mantle viscosity according to Dumoulin et al., 2017 (right green box) is compared with the
 348 experiment capability (left green box, here shown at 5 times the formal uncertainty) showing the
 349 possibility to constrain the interior structure of Venus to unprecedented accuracy.

350

351 5 Conclusions

352 By simulating the nominal mission scenario of the proposed VERITAS mission to Venus,
 353 we showed that VERITAS will be able to determine with very good accuracy the physical
 354 parameters needed to build a detailed understanding of the planet's interior structure. The precise
 355 characterization of the tidal response of Venus via the measurement of its complex Love number
 356 will allow to place tight constraints on the state of the core and on the viscous response of the
 357 planet. The combined processing of Earth Doppler tracking and VISAR data proves to be
 358 extremely effective in the determination of the rotational state of the planet and the moment of
 359 inertia factor, further extending the possibility of understanding of the dynamical evolution of
 360 Earth's neighboring planet. These fundamental quantities, which are little known so far, are
 361 necessary to understand the formation of Venus and its thermal and magnetic evolution - also in
 362 the context of the other terrestrial planets. Ultimately they can provide valuable clues as to how
 363 and why Venus evolved into an uninhabitable planet.

364 **Acknowledgments, Samples, and Data**

365 The work of G.C, F.D.M, P.R., D.D and L.I. has been supported by the Italian Space Agency
366 (ASI) contract 2020-15-HH.0.

367 A portion of this research was conducted at the Jet Propulsion Laboratory, California Institute of
368 Technology, under contract with the National Aeronautics and Space Administration. The
369 information presented about VERITAS is pre-decisional and is provided for planning and
370 discussion purposes only.

371 Data were not used, nor created for this research.

372

373 **References**

374 Saunders, R. S., Spear, A. J., Allin, P. C., Austin, R. S., Berman, A. L., Chandler, R. C., Clark,
375 J., Decharon, A. V., De Jong, E. M., Griffith, D. G., Gunn, J. M., Hensley, S., Johnson, W.
376 T. K., Kirby, C. E., Leung, K. S., Lyons, D. T., Michaels, G. A., Miller, J., Morris, R. B., ...
377 Wall, S. D. (1992). Magellan mission summary. *Journal of Geophysical Research*, 97(E8),
378 13067. <https://doi.org/10.1029/92JE01397>

379 Ford, P. G., & Pettengill, G. H. (1992). Venus topography and kilometer-scale slopes. *Journal of*
380 *Geophysical Research*, 97(E8), 13103. <https://doi.org/10.1029/92JE01085>

381 Campbell, B. A., Campbell, D. B., Carter, L. M., Chandler, J. F., Giorgini, J. D., Margot, J. L.,
382 Morgan, G. A., Nolan, M. C., Perillat, P. J., & Whitten, J. L. (2019). The mean rotation rate
383 of Venus from 29 years of Earth-based radar observations. *Icarus*.
384 <https://doi.org/10.1016/j.icarus.2019.06.019>

385 Hensley, S., Campbell, B., Perkovic-Martin, D., Wheeler, K., Kiefer, W., Ghail, R. (2020)
386 "VISAR and VenSAR: Two Proposed Radar Investigations of Venus," *IEEE Radar Conference*
387 *(RadarConf20)*, Florence, Italy, 2020, <http://10.1109/RadarConf2043947.2020.9266323>

388 Aitta, A. (2012). Venus' internal structure, temperature and core composition. *Icarus*, 218(2),
389 967–974. <https://doi.org/10.1016/j.icarus.2012.01.007>

390 Yoder, C. F. (1995). Venus' Free Obliquity. *Icarus*, 117(2), 250–286.
391 <https://doi.org/10.1006/icar.1995.1156>

392 Helbert, J., Säuberlich, T., Dyar, M. D., Ryan, C., Walter, I., Réess, J.-M., et al. (2020). The
393 Venus Emissivity Mapper (VEM): advanced development status and performance
394 evaluation. In M. Strojnik (Ed.), *Infrared Remote Sensing and Instrumentation XXVIII* (p.
395 6). SPIE. <https://doi.org/10.1117/12.2567634>

396 Cappuccio, P., Notaro, V., Di Ruscio, A., Iess, L., Genova, A., Durante, D., et al. (2020). Report
397 on first inflight data of BepiColombo's Mercury Orbiter Radio-science Experiment. *IEEE*

- 398 *Transactions on Aerospace and Electronic Systems*, 1–1.
399 <https://doi.org/10.1109/TAES.2020.3008577>
- 400 Bertotti, B., Comoretto, G., & Iess, L. (1993). Doppler tracking of spacecraft with multi-
401 frequency links. *Astronomy and Astrophysics*, 269(1–2), 608–616.
- 402 Iess, L., Folkner, W. M., Durante, D., Parisi, M., Kaspi, Y., Galanti, E., et al. (2018).
403 Measurement of Jupiter’s asymmetric gravity field. *Nature*, 555(7695), 220–222.
404 <https://doi.org/10.1038/nature25776>
- 405 Durante, D., Parisi, M., Serra, D., Zannoni, M., Notaro, V., Racioppa, P., et al. (2020). Jupiter’s
406 Gravity Field Halfway Through the Juno Mission. *Geophysical Research Letters*, 47(4).
407 <https://doi.org/10.1029/2019GL086572>
- 408 Mazarico, E., Genova, A., Goossens, S., Lemoine, F. G., Neumann, G. A., Zuber, M. T., Smith,
409 D. E., & Solomon, S. C. (2014). The gravity field, orientation, and ephemeris of Mercury
410 from MESSENGER observations after three years in orbit. *Journal of Geophysical*
411 *Research: Planets*, 119(12), 2417–2436. <https://doi.org/10.1002/2014JE004675>
- 412 Konopliv, A. S., Park, R. S., Yuan, D.-N., Asmar, S. W., Watkins, M. M., Williams, J. G.,
413 Fahnestock, E., Kruizinga, G., Paik, M., Strelakov, D., Harvey, N., Smith, D. E., & Zuber,
414 M. T. (2013). The JPL lunar gravity field to spherical harmonic degree 660 from the
415 GRAIL Primary Mission. *Journal of Geophysical Research: Planets*, 118(7), 1415–1434.
416 <https://doi.org/10.1002/jgre.20097>
- 417 Konopliv, A. S., Banerdt, W. B., & Sjogren, W. L. (1999). Venus Gravity: 180th Degree and
418 Order Model. *Icarus*, 139(1), 3–18. <https://doi.org/10.1006/icar.1999.6086>
- 419 Konopliv, A. S., & Yoder, C. F. (1996). Venusian k₂ tidal Love number from Magellan and
420 PVO tracking data. *Geophysical Research Letters*, 23(14), 1857–1860.
421 <https://doi.org/10.1029/96GL01589>
- 422 Müller-Wodarg, I. C. F., Bruinsma, S., Marty, J.-C., & Svedhem, H. (2016). In situ observations
423 of waves in Venus’s polar lower thermosphere with Venus Express aerobraking. *Nature*
424 *Physics*, 12(8), 767–771. <https://doi.org/10.1038/nphys3733>
- 425 Kliore, A. J., Keating, G. M., & Moroz, V. I. (1992). Venus international reference atmosphere
426 (1985). *Planetary and Space Science*, 40(4), 573. [https://doi.org/10.1016/0032-0633\(92\)90255-M](https://doi.org/10.1016/0032-0633(92)90255-M)
427
- 428 Bills, B. G., Navarro, T., Schubert, G., Ermakov, A., & Górski, K. M. (2020). Gravitational
429 signatures of atmospheric thermal tides on Venus. *Icarus*, 340, 113568.
430 <https://doi.org/10.1016/j.icarus.2019.113568>

- 431 Cottureau, L., & Souchay, J. (2009). Rotation of rigid Venus: a complete precession-nutation
432 model. *Astronomy & Astrophysics*, 507(3), 1635–1648. [https://doi.org/10.1051/0004-
433 6361/200912174](https://doi.org/10.1051/0004-6361/200912174)
- 434 Dumoulin, C., Tobie, G., Verhoeven, O., Rosenblatt, P., & Rambaux, N. (2017). Tidal
435 constraints on the interior of Venus. *Journal of Geophysical Research: Planets*, 122(6),
436 1338–1352. <https://doi.org/10.1002/2016JE005249>
- 437 Genova, A., Goossens, S., Lemoine, F. G., Mazarico, E., Neumann, G. A., Smith, D. E., &
438 Zuber, M. T. (2016). Seasonal and static gravity field of Mars from MGS, Mars Odyssey
439 and MRO radio science. *Icarus*, 272, 228–245. <https://doi.org/10.1016/j.icarus.2016.02.050>
- 440 Frankot, R. T., Hensley, S., & Shafer, S. (1994). Noise resistant estimation techniques for SAR
441 image registration and stereo matching. In *Proceedings of IGARSS '94 - 1994 IEEE
442 International Geoscience and Remote Sensing Symposium* (Vol. 2, pp. 1151–1153). IEEE.
443 <https://doi.org/10.1109/IGARSS.1994.399369>
- 444 Davies, M. E., Colvin, T. R., Rogers, P. G., Chodas, P. W., Sjogren, W. L., Akim, E. L., et al.
445 (1992). The rotation period, direction of the North Pole, and geodetic control network of
446 Venus. *Journal of Geophysical Research*, 97(E8), 13141.
447 <https://doi.org/10.1029/92JE01166>
- 448 Iess, L., Asmar, S.W., Cappuccio, P. et al. Gravity, Geodesy and Fundamental Physics with
449 BepiColombo's MORE Investigation. *Space Science Reviews* 217, 21 (2021).
450 <https://doi.org/10.1007/s11214-021-00800-3>
- 451 Iess, L., Asmar, S., & Tortora, P. (2009). MORE: An advanced tracking experiment for the
452 exploration of Mercury with the mission BepiColombo. *Acta Astronautica*.
453 <https://doi.org/10.1016/j.actaastro.2009.01.049>
- 454 Evans, S., Taber, W., Drain, T., Smith, J., Wu, H.-C., Guevara, M., et al. (2018). MONTE: the
455 next generation of mission design and navigation software. *CEAS Space Journal*, 10(1), 79–
456 86. <https://doi.org/10.1007/s12567-017-0171-7>
- 457 Archinal, B. A., A'Hearn, M. F., Bowell, E., Conrad, A., Consolmagno, G. J., Courtin, R., ...
458 Williams, I. P. (2011). Report of the IAU Working Group on Cartographic Coordinates and
459 Rotational Elements: 2009. *Celestial Mechanics and Dynamical Astronomy*, 109(2), 101–
460 135. <https://doi.org/10.1007/s10569-010-9320-4>
- 461 Murray, C. D., & Dermott, S. F. (2000). *Solar System Dynamics*. In *Solar System Dynamics*.
462 Cambridge University Press. <https://doi.org/10.1017/CBO9781139174817>
- 463 Simon, J. L., Bretagnon, P., Chapront, J., Chapront-Touze, M., Francou, G., Laskar, J. (1994).
464 Numerical expressions for precession formulae and mean elements for the Moon and the planets.
465 *Astron. Astrophys.* 282, 663-683 . <https://ui.adsabs.harvard.edu/abs/1994A&A...282..663S>

- 466 Smrekar, S. and the VERITAS science team, VERITAS (Venus Emissivity, Radio Science,
467 INSAR, Topography And Spectroscopy): A Proposed Discovery Mission, Lunar Plan. Sci.
468 Conf, Abstract #, 2021.
- 469 Garate-Lopez, I., & Lebonnois, S. (2018). Latitudinal variation of clouds' structure responsible
470 for Venus' cold collar. *Icarus*. <https://doi.org/10.1016/j.icarus.2018.05.011>
- 471 Freeman, A., & Smrekar, S. E. (2015). VERITAS – a Discovery-class Venus surface geology
472 and geophysics mission. In *11th Low Cost Planetary Missions Conference*.
- 473 Goossens, S., Mazarico, E., Rosenblatt, P., Lebonnois, S., & Lemoine, F. (2018, November).
474 Venus Gravity Field Determination Using Magellan and Venus Express Tracking Data. In
475 *16th Meeting of the Venus Exploration and Analysis Group (VEXAG)* (Vol. 16, No. 2137, p.
476 8029).
- 477 Goossens, S., Lemoine, F. G., Rosenblatt, P., Lebonnois, S., & Mazarico, E. (2017, March).
478 Venus Gravity Field Modeling from Magellan and Venus Express Tracking Data. In *Lunar
479 and Planetary Science Conference* (No. 1964, p. 1984)
- 480 Petrov, L. (2004). Study of the atmospheric pressure loading signal in very long baseline
481 interferometry observations. *Journal of Geophysical Research*, *109*(B3), B03405.
482 <https://doi.org/10.1029/2003JB002500>
- 483 Rivoldini, A., Van Hoolst, T., Verhoeven, O., Mocquet, A., & Dehant, V. (2011). Geodesy
484 constraints on the interior structure and composition of Mars. *Icarus*, *213*(2), 451–472.
485 <https://doi.org/10.1016/j.icarus.2011.03.024>

486
487

Geophysical Research Letters

Supporting Information for

The Determination of the Rotational State and Interior Structure of Venus with VERITAS

G. Cascioli¹, S. Hensley², F. De Marchi¹, D. Breuer³, D. Durante¹, P. Racioppa¹, L. Iess¹, E. Mazarico⁴
and S. E. Smrekar²

¹Department of Mechanical and Aerospace Engineering, Sapienza University of Rome, Rome, Italy.

²Jet Propulsion Laboratory, California Institute of Technology, Pasadena, CA, USA.

³Institute for Planetary Research, German Aerospace Center (DLR), Berlin, Germany.

⁴NASA Goddard Space Flight Center, Greenbelt, MD, USA

Contents of this file

Text S1 to S4
Figures S1 to S2
Table S1

Delete all unused file types below. Copy/paste for multiples of each file type as needed.

Text S1: Effect of the number of landmarks.

To explore the effectiveness of the inclusion of radar tie points, we performed a sensitivity analysis of the results to the number of included landmarks. In Figure S1 we report the formal uncertainty improvement factor as a function of the number of observed landmark. Not surprisingly, the improvement factor P depends on the number of landmarks n as:

$$P(n) \sim n^{\frac{1}{2}}$$

A consequence of the assumption that the measurements are statistically independent. The results that we report can be easily scaled to an arbitrary higher number of landmarks. The increase in the accuracy of the rotational parameters, MOIF and k_2 shows that, while the bulk of the information matrix comes from radio tracking data, tie points, being a largely independent data set, increase the overall information content by a quite significant amount.

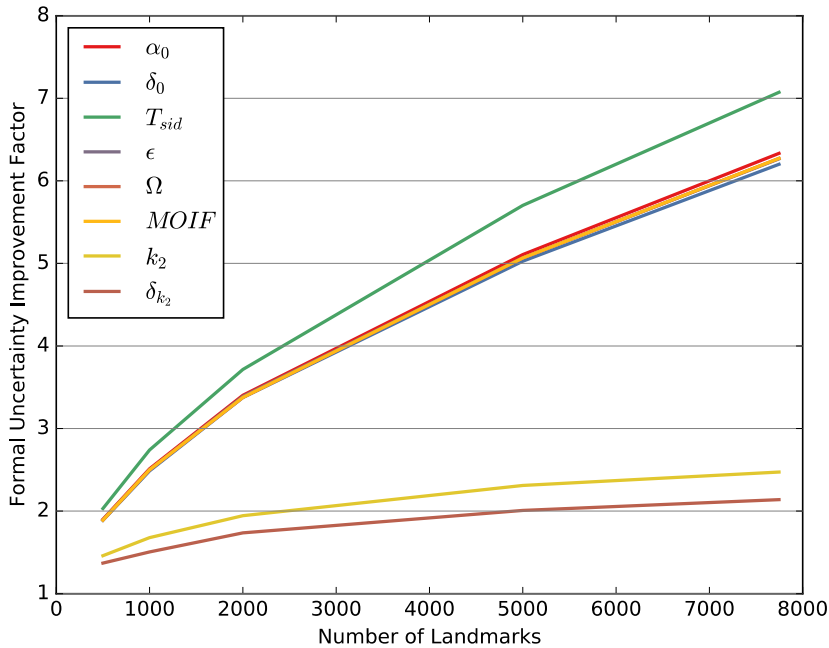


Figure S1 Tie points improvement factor as a function of the number of observed landmarks for the physical quantities object of our analysis

Text S2: Thermal tides modeling.

In the dynamical model used in our simulations we included the effect of atmospheric thermal tides. As shown by Bills et al., (2020) the mass transport induced by solar heating of the atmosphere is not a negligible factor for high precision radioscience experiments at Venus. For a realistic assessment of the attainable accuracies of VERITAS, we modeled the time-variable gravity field induced by solar heating-driven pressure variations of the atmosphere.

The spherical harmonics expansion of the total (static plus atmosphere) gravity field can be written as a function of time t as:

$$C_{lm}(t) = C_{lm}^S + \Delta C_{lm}(t) \quad (S2.1)$$

C_{lm} is the total C coefficient of degree l and order m of the gravity field, C_{lm}^S is the static coefficient and $\Delta C_{lm}(t)$ is the correction due to the time variable mass transport (the same formulation applies for S_{lm} coefficients, here omitted for brevity).

To determine the time variable atmospheric contribution, we employed the model developed by Garate-Lopez and Lebonnois (2018) for retrieving surface pressure variations induced by solar heating and then converted these perturbations in the associated gravity field coefficient with a technique originally developed for Earth (Petrov, 2004) and applied also on Mars (Genova et al., 2016)). This procedure produces the time series of spherical harmonics expansions of the atmospheric gravity field. The gravity field perturbation induced by solar heating is a periodic signal of fundamental frequency f_1 , equal to the main forcing effect (i.e. Venus solar day ~ 116 days). We isolated the contribution of the fundamental frequency and its 3 first harmonics via a Fourier transform. Thus, we can expand equation (S2.1) as:

$$C_{lm}(t) = C_{lm}^S + \sum_n \Delta C_{lm}^n(t)$$

$$\Delta C_{lm}^n = A_{C_{lm}}^n \cos(2\pi f_n t) + B_{C_{lm}}^n \sin(2\pi f_n t)$$

Where $f_n = n f_0$ with $n = 1, 2, 3, 4$ and A, B are coefficients derived from the Fourier analysis specific for each coefficient, degree and order.

In our simulations we assessed the necessity of including these effects in the dynamical model of VERITAS as its extremely precise tracking system is sensitive to the main components of the thermal tides perturbation. In particular, we have assessed that if thermal tides are not accounted for, significant biases might arise in the gravity field and rotational state solution, in particular affecting the Love number k_2 . The most recent works about Venus gravity field accounted for the atmospheric contribution by forward modelling its effect (Goossens et al., 2017, Goossens et al., 2018). We have chosen to adopt a conservative approach and account for the intrinsic uncertainty of the atmospheric model. We have chosen to model the thermal tide field up to the degree and order that guarantees that the higher degrees produce no residual signal in the Doppler residuals (i.e. degree and order 18 for f_1 , 13 for f_2 , 7 for f_3 and 10 for f_4) and considered the uncertainty associated to the correction coefficients

$A_{C_{lm}}^f, A_{S_{lm}}^f, B_{C_{lm}}^f, B_{S_{lm}}^f$ for the frequencies f_1 through f_4 .

In our simulation we evaluated the effect on the solution of the assumed apriori knowledge of the atmospheric model, without delving into a detailed analysis of atmospheric dynamics. In particular, we explored three cases by setting different apriori uncertainties on the thermal tides parameters. We considered an accurate model (model uncertainty equal to 10%), a medium-accuracy model (50% accuracy) and a coarse-accuracy model (100% accuracy). In table S1 we report the results relative to each of the three assumptions. It is important to note how the results, when combining tie points radar observation, become significantly less sensitive to the accuracy of the model, for all the parameters except the tidal response which, not surprisingly, is significantly sensitive to the atmospheric tides.

Table S1 Results comparison (In terms of formal uncertainties, 3σ) for different levels of apriori knowledge of the atmospheric thermal tides model parameters

Parameter	10%		50%		100%	
	Earth Doppler Only	Tie Points	Earth Doppler Only	Tie Points	Earth Doppler Only	Tie Points
α_0 [arcsec]	2.3	0.36	2.9	0.39	3.1	0.39
δ_0 [arcsec]	1.3	0.21	1.6	0.21	1.8	0.21
T_{sid} [day]	1.1×10^{-5}	1.5×10^{-6}	1.3×10^{-6}	1.6×10^{-5}	1.4×10^{-5}	1.6×10^{-5}
ϵ [arcsec]	1.0	0.16	1.3	0.17	1.4	0.17
Ω [deg/century]	3.2×10^{-2}	5.1×10^{-3}	3.9×10^{-2}	5.4×10^{-3}	4.3×10^{-2}	5.4×10^{-3}
$MOIF$	8.6×10^{-3}	1.4×10^{-3}	1.1×10^{-2}	1.4×10^{-3}	1.2×10^{-2}	1.4×10^{-3}
k_2	9.6×10^{-4}	3.9×10^{-4}	1.4×10^{-3}	7.8×10^{-4}	1.8×10^{-3}	1.3×10^{-3}
δ_{k_2} [deg]	8.6×10^{-2}	4.0×10^{-2}	1.6×10^{-1}	1.3×10^{-1}	2.5×10^{-1}	2.2×10^{-1}

Text S3. Uncertainty on Venus' MOIF from pole precession measurements

In this section we will obtain the equations to express the motion of the pole as a function of the equatorial coordinates and their time derivatives. Finally, we will show the relation arising between these latter quantities after neglecting the nutations. This relation will be used in the simulations as a constraint to improve the measurement of the precession rate and the MOIF. The Venus ecliptic (V_E) and the (usual) Earth ecliptic (E_E) reference frames are represented by the unit vectors $\{\mathbf{u}_{v,x}, \mathbf{u}_{v,y}, \mathbf{u}_{v,z}\}$ and $\{\mathbf{u}_{E,x}, \mathbf{u}_{E,y}, \mathbf{u}_{E,z}\}$ respectively. The equatorial frame is represented by $\{\mathbf{u}_{eq,x}, \mathbf{u}_{eq,y}, \mathbf{u}_{eq,z}\}$.

We will use the following coordinates:

- $\alpha(t), \delta(t)$ are right ascension and declination (equatorial J2000 coordinates);
- $\lambda(t), \beta(t)$ are ecliptic coordinates referred to the E_E reference frame at J2000.0;
- $\lambda_V(t), \beta_V(t)$ are ecliptic coordinates referred to the V_E reference frame at J2000.0

We define:

- the direction (as a unit vector) P_V of the Venus' pole;
- the direction (as a unit vector) P_{OV} of the normal to the Venus orbital plane (hereafter the "orbital pole").

All coordinates above will be referred to the pole position (in particular, $\beta_V(t)$ is the nutation in obliquity and $\lambda_V(t)$ is the sum of the precession and the nutation in longitude.

The direction P_V in the three reference frames is:

$$P_{V,eq} = \cos[\delta(t)]\cos[\alpha(t)]\mathbf{u}_{eq,x} + \cos[\delta(t)]\sin[\alpha(t)]\mathbf{u}_{eq,y} + \sin[\delta(t)]\mathbf{u}_{eq,z} \quad (S3.1)$$

$$P_{V,E_E} = \cos[\beta(t)]\cos[\lambda(t)]\mathbf{u}_{E,x} + \cos[\beta(t)]\sin[\lambda(t)]\mathbf{u}_{E,y} + \sin[\beta(t)]\mathbf{u}_{E,z} \quad (S3.2)$$

$$P_{V,V_E} = \cos[\beta_V(t)]\cos[\lambda_V(t)]\mathbf{u}_{V,x} + \cos[\beta_V(t)]\sin[\lambda_V(t)]\mathbf{u}_{V,y} + \sin[\beta_V(t)]\mathbf{u}_{V,z} \quad (S3.3)$$

while the orbital pole direction in the E_E frame is

$$P_{0V,E_E} = \sin i_0 \sin \Omega_0 \mathbf{u}_{E,x} - \sin i_0 \cos \Omega_0 \mathbf{u}_{E,y} + \cos i_0 \mathbf{u}_{E,z} \quad (S3.4)$$

where $i_0 = 3.39466189^\circ$ (inclination) and $\Omega_0 = 76.67992019^\circ$ (longitude of the ascending node), at J2000.0 (Simon et al., 1994).

The transformations of P_V from equatorial to E_E (and vice versa) coordinates are

$$P_{V,E_E} = R^{-1}P_{V,eq} \quad \text{and} \quad P_{V,eq} = RP_{V,E_E} \quad (S3.5)$$

where

$$R = \begin{pmatrix} 1 & 0 & 0 \\ 0 & \cos \epsilon & -\sin \epsilon \\ 0 & \sin \epsilon & \cos \epsilon \end{pmatrix} \quad (S3.6)$$

and $\epsilon = 23.43662deg$ is the Earth's obliquity.

Eq. 3.5 corresponds to

$$\cos \beta \cos \lambda = \cos \alpha \cos \delta \quad (S3.7)$$

$$\cos \beta \sin \lambda = \cos \epsilon \cos \delta \sin \alpha + \sin \epsilon \sin \delta \quad (S3.8)$$

$$\sin \beta = \cos \epsilon \sin \delta - \sin \epsilon \cos \delta \sin \alpha \quad (S3.9)$$

At J2000.0 ($t = 0$) the equatorial coordinates of the pole of Venus are $\alpha_0 = \alpha(0) 272.76^\circ$ and $\delta_0 = \delta(0) = 67.16^\circ$ (Archinal et al., 2009).

By solving Equations 3.7-3.9, we obtain the pole position at the same epoch in E_E coordinates:

$$\lambda_0 = 30.079869^\circ ; \quad \beta_0 88.762332^\circ \quad (S3.10)$$

The $\mathbf{u}_{V,x}$, $\mathbf{u}_{V,y}$, $\mathbf{u}_{V,z}$ directions of the V_E reference frame are:

- The z-axis points towards the pole $\mathbf{u}_{V,z} = P_V$;

- The x-axis is the direction of the vernal equinox of Venus: the vernal equinox of Venus coincides with the coordinates of the ascending node of the orbit of Venus at J2000.0 with respect to the equator of Venus at the same date, so $\mathbf{u}_{V,x} = P_{0V} \times P_V$

From Equations 3.2 and 3.4 we obtain

$$\mathbf{u}_{V,x} = u_{V,x_1} \mathbf{u}_{E,x} + u_{V,x_2} \mathbf{u}_{E,y} + u_{V,x_3} \mathbf{u}_{E,z} \quad (\text{S3.11})$$

Where

$$u_{V,x_1} = \frac{\cos \beta_0 \cos i_0 \sin \lambda_0 + \sin \beta_0 \sin i_0 \cos \Omega_0}{\sqrt{1 - [\sin \beta_0 \cos i_0 - \cos \beta_0 \sin i_0 \cos(\lambda_0 - \Omega_0)]^2}} \quad (\text{S3.12})$$

$$u_{V,x_2} = \frac{\sin \beta_0 \sin i_0 \sin \Omega_0 - \cos \beta_0 \cos i_0 \cos \lambda_0}{\sqrt{1 - [\sin \beta_0 \cos i_0 - \cos \beta_0 \sin i_0 \cos(\lambda_0 - \Omega_0)]^2}} \quad (\text{S3.13})$$

$$u_{V,x_3} = -\frac{\cos \beta_0 \sin i_0 \cos(\lambda_0 - \Omega_0)}{\sqrt{1 - [\sin \beta_0 \cos i_0 - \cos \beta_0 \sin i_0 \cos(\lambda_0 - \Omega_0)]^2}} \quad (\text{S3.14})$$

and

$$\mathbf{u}_{V,z} = u_{V,z_1} \mathbf{u}_{E,x} + u_{V,z_2} \mathbf{u}_{E,y} + u_{V,z_3} \mathbf{u}_{E,z} \quad (\text{S3.15})$$

with

$$u_{V,z_1} = \sin i_0 \sin \Omega_0 ; u_{V,z_2} = -\sin i_0 \cos \Omega_0 ; u_{V,z_3} = \cos i_0 \quad (\text{S3.16})$$

and finally, $\mathbf{u}_{V,y} = \mathbf{u}_{V,z} \times \mathbf{u}_{V,x}$.

We define M (at J2000.0) as

$$M = \begin{pmatrix} u_{V,x_1} & u_{V,y_1} & u_{V,z_1} \\ u_{V,x_2} & u_{V,y_2} & u_{V,z_2} \\ u_{V,x_3} & u_{V,y_3} & u_{V,z_3} \end{pmatrix} \approx \begin{pmatrix} 0.531509 & -0.84509 & 0.0576204 \\ 0.846837 & 0.531678 & -0.0136422 \\ -0.0191066 & 0.0560461 & 0.998245 \end{pmatrix} \quad (\text{S3.17})$$

The $\alpha(t)$ and $\delta(t)$ coordinates as functions of $\beta_V(t)$, λ_V are given by the following relations

$$P_{V,eq}(t) = RMP_{V,V_E}(t) \quad P_{V,V_E}(t) = M^{-1}R^{-1}P_{V,eq}(t) \quad (\text{S3.18})$$

The pole motion around the orbit pole is (t=0 corresponds to J2000.0)

$$\lambda_V(t) = \lambda_V(0) + \Omega t + \delta\lambda_V(t) \quad (\text{S3.19})$$

$$\beta_V(t) = \beta_V(0) + \delta\beta_V(t) \quad (\text{S3.20})$$

where $\delta\beta_V$, $\delta\lambda_V$ are the nutations in obliquity and in longitude, respectively and Ω is the precession rate of the Venus pole. The precession rate is the sum of the solar precession ($\sim 44.74''/\text{yr}$) and the planetary precession ($-10''/\text{yr}$, Simon et al 1994). By solving for β_V in Eq. (S3.18b) we get

$$\beta_V(0) = 87.3638^\circ; \lambda_V(0) = 90^\circ \quad (\text{S3.21})$$

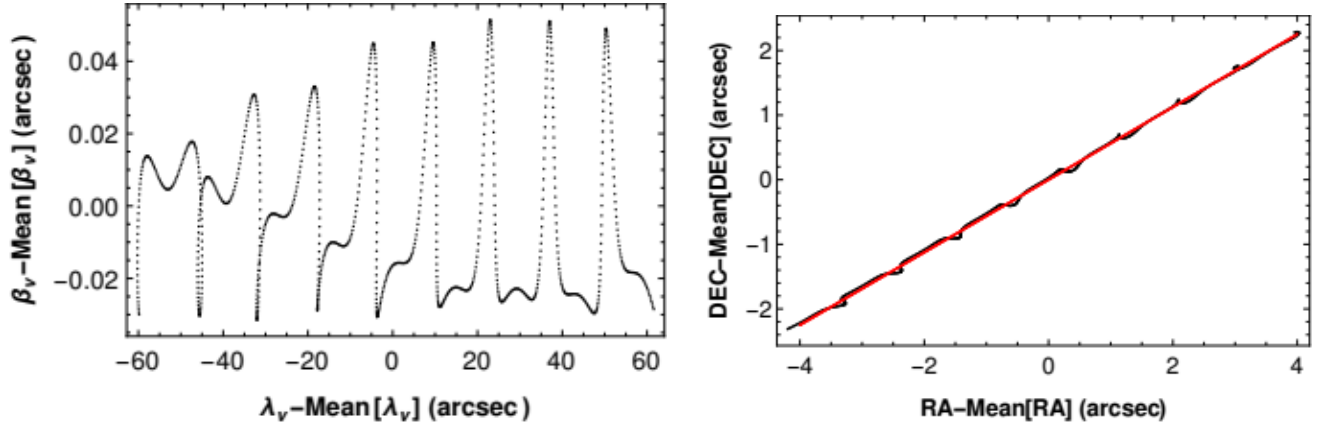


Figure S2. Left: longitude vs. obliquity nutations and precession about the orbit pole (time span: 4 Venus cycles, 972d). The displacement in longitude is about 45''/yr. However, the overall displacement in the sky is very small. Right: the same path but in equatorial coordinates over the same interval of time (red: precession only, black: precession and nutations).

By deriving Eq. (18b) with respect to time and neglecting the nutations, we get

$$\begin{aligned} \frac{\dot{\alpha}(t)}{\dot{\delta}(t)} &= \frac{\sin \alpha(t) \tan \delta(t) (\cos \epsilon \sin i_0 \cos \Omega_0 + \sin \epsilon \cos i_0)}{\cos \alpha(t) (\cos \epsilon \sin i_0 \cos \Omega_0 + \sin \epsilon \cos i_0) + \sin i_0 \sin \Omega_0 \sin \alpha(t)} + \\ &+ \frac{\cos \epsilon \cos i_0 - \sin i_0 (\sin \Omega_0 \cos \alpha(t) \tan \delta(t) + \sin \epsilon \cos \Omega_0)}{\cos \alpha(t) (\cos \epsilon \sin i_0 \cos \Omega_0 + \sin \epsilon \cos i_0) + \sin i_0 \sin \Omega_0 \sin \alpha(t)} \end{aligned} \quad (\text{S3.22})$$

This quantity depends on the geometry of the orbit (i_0, Ω_0) and on the pole position but it is independent of Ω .

The link between $\frac{d\alpha}{dt}$ and $\frac{d\delta}{dt}$ is a consequence of the circular path of the pole. For $t = 0$ (i.e. at J2000.0) we obtain

$$\dot{\alpha}(0) = 1.77694 \dot{\delta}(0) \quad (\text{S3.23})$$

From Eq (18a) we get

$$\begin{aligned} \cos \delta \cos \alpha &= u_{V,x_1} \cos \beta_V \cos \lambda_V + u_{V,y_2} \cos \beta_V \sin \lambda_V + u_{V,z_1} \sin \beta_V \\ (\text{S3.24}) \\ \cos \delta \sin \alpha &= \cos \epsilon (u_{V,x_2} \cos \beta_V \cos \lambda_V + u_{V,y_2} \cos \beta_V \sin \lambda_V + u_{V,z_2} \sin \beta_V) - \\ \sin \epsilon (u_{V,x_3} \cos \beta_V \cos \lambda_V + u_{V,y_3} \cos \beta_V \sin \lambda_V + u_{V,z_3} \sin \beta_V) \end{aligned} \quad (\text{S3.25})$$

$$\sin \delta = \cos \beta_V \cos \lambda_V (u_{V,x_2} \sin \epsilon + u_{V,x_3} \cos \epsilon) + \cos \beta_V \sin \lambda_V (u_{V,y_2} \sin \epsilon + u_{V,y_3} \cos \epsilon) + \sin \beta_V (u_{V,z_2} \sin \epsilon + u_{V,z_3} \cos \epsilon) \quad (\text{S3.26})$$

The functions $\alpha(t)$, $\delta(t)$, obtained by solving Eqs. S3.24-S3.26, can be expanded to first order in Taylor series around the pole position. We get (units are radians)

$$\alpha(t) \approx -1.52263 + 2.11423\delta\beta_V(t) - 0.0672264(\delta\lambda_V(t) + \Omega t) \quad (\text{S3.27})$$

$$\delta(t) \approx 1.17216 - 0.568672\delta\beta_V(t) - 0.0378326(\delta\lambda_V(t) + \Omega t) \quad (\text{S3.28})$$

Finally, we obtain the components of the initial velocity of the pole. The evolution of the Venus' orbital elements due to planetary effects are already included in our setup, so here we will consider the solar precession rate only.

Moreover, we neglect the nutations since, to our purposes, they are fast and zero-mean oscillations. Therefore, neglecting the nutations, the relations between $\dot{\alpha}$, $\dot{\delta}$ and Ω :

$$\dot{\alpha}(0) \approx -0.0672264\Omega = -4.62097 \times 10^{-13} [\text{rad/s}] \quad (\text{S3.29})$$

$$\dot{\delta}(0) \approx -0.0378326\Omega = -2.60051 \times 10^{-13} [\text{rad/s}] \quad (\text{S3.30})$$

Finally, the ratio $\dot{\alpha}(0)/\dot{\delta}(0)$ (Eq. 22) can be used as an a priori constraint between the two quantities.

Text S4. Tie points simulation

The match covariance matrix is given by

$$M_{cov} = k_c H^{-1} \left(2\sigma_n^2 H + \frac{1}{2} A_w \sigma_n^4 I \right) H^{-1} \quad (\text{S4.1})$$

Where k_c is an empirical constant inferred from Magellan match statistics, I is the identity matrix, H is the hessian of the match correlation function $c(x, y)$. For a given image offset (x, y) the hessian is given by

$$H = \begin{bmatrix} \frac{\partial^2 c}{\partial x^2} & \frac{\partial^2 c}{\partial x \partial y} \\ \frac{\partial^2 c}{\partial x \partial y} & \frac{\partial^2 c}{\partial y^2} \end{bmatrix} \quad (\text{S4.2})$$

A_w is the area in pixel of the marching window, σ_n is a measure of the backscatterer difference between the two images in the matching window

$$\sigma_n = \frac{1}{2A_w} \sum_{x \in W} [I_1(\vec{x}) - \bar{I}_1 - I_2(\vec{x} - \vec{\delta}) + \bar{I}_2(\vec{\delta})]^2 \quad (\text{S4.3})$$

where $I_1(\vec{x})$ and $I_2(\vec{x})$ are the pixel intensities for the two images at position \vec{x} , $\vec{\delta}$ is the offset vector between the images, and \bar{I}_1 and $\bar{I}_2(\vec{\delta})$ are mean intensities in the match window. We approximate the correlation function for a good match by the product of *sinc* functions given by:

$$c(x, y) = \text{sinc} \left[\frac{\pi x}{2\sigma_{m_x}} \right] \text{sinc} \left[\frac{\pi y}{2\sigma_{m_y}} \right] \quad (\text{S4.4})$$

where σ_{m_x} and σ_{m_y} are the matching accuracy in pixel in the x and y directions. Differentiating Equation S4.4 twice and evaluating at the peak yields

$$H = \begin{bmatrix} -\frac{1}{12} \frac{\pi^2}{\sigma_{m_x}^2} & 0 \\ 0 & -\frac{1}{12} \frac{\pi^2}{\sigma_{m_y}^2} \end{bmatrix} \quad (\text{S4.5})$$

where σ_{m_x} and σ_{m_y} are given by

$$\sigma_{m_q} = \frac{1}{2} - k_{m_q} \frac{\sigma_{10 \times 10}}{\bar{\sigma}_{10 \times 10} \frac{1}{\sqrt{N_L}} (1 + \frac{1}{SNR})} \quad (\text{S4.6})$$

where $q = x, y$, k_{m_q} are empirical parameters based on Magellan match statistics, SNR is the signal to noise ratio, N_L are the number of looks (number of single look pixel intensities averaged together in a 30 m multi-looked pixel to reduce thermal and speckle noise, $\bar{\sigma}_{10 \times 10}$, $\sigma_{\sigma_{10 \times 10}}$ are the mean and standard deviation of the backscatter in a 10 by 10 pixel window centered at the match point obtained from Magellan imagery and where

$$SNR = \frac{\bar{\sigma}_{10 \times 10}}{NES0} \quad (\text{S4.6})$$

where $NES0$ is the radar noise equivalent sigma naught (backscatter value where the SNR equals to 1). To obtain an approximate value for σ_n^2 we use the

$$\sigma_n^2 = \left[\sqrt{2} \bar{\sigma}_{10 \times 10} \left(\frac{1}{\sqrt{N_L}} \frac{1}{SNR} + k_s \frac{\bar{\sigma}_v}{\sigma_{10 \times 10}} \right) \right] \quad (\text{S4.7})$$

where k_s is an empirical value derived from Magellan match statistics and $\bar{\sigma}_v$ is the mean X-band backscatter value for Venus, roughly -10.5 dB.